Optics Letters

# Lab-on-fiber: laser-induced micro-cavity for a relative humidity measurement

Jiabin Wang,[1] Yanru Kou,[1] Anzhi Wang,[1] Jiayu Hao,[1] Chong Niu,[1] Hang Jiang,[1] Haoran Meng,[2] Weimin Sun,[1] and Tao Geng[1,3,*]

[1]Key Laboratory of In-Fiber Integrated Optics of Ministry of Education, Harbin Engineering University, Harbin 150001, China
[2]Changchun Institute of Optics, Fine Mechanics and Physics, Chinese Academy of Sciences, ChangChun 130033, China
[3]State Key Laboratory of Applied Optics, Changchun Institute of Optics, Fine Mechanics and Physics, Chinese Academy of Sciences, Changchun 130033, China
*gengtao_hit_oe@126.com

Received 14 July 2023; revised 12 September 2023; accepted 20 September 2023; posted 20 September 2023; published 3 October 2023

**The lab-on-fiber design philosophy is the foundation for creating high-performance integrated fiber sensors. Hence, this Letter proposes an ultra-compact Fabry–Perot interferometer (FPI) based on a laser-induced micro-cavity (LIMC-FPI) on a fiber end for measuring relative humidity. To our knowledge, this novel approach, named the fiber-end photopolymerization (FEP) technique, is applied to create a micro-cavity. Specifically, a pair of humidity-sensitive polymer pillars and a resin end cap obtained by FEP are integrated to generate the cavity. As the ambient humidity changes, the pillars lengthen or shorten, resulting in the spectral evolution of the LIMC-FPI. A typical humidity sensitivity of 0.18 nm/%RH is obtained experimentally. For monitoring the human breathing process, the LIMC-FPI is responsive in the breathing frequency range of 0.2 to 0.5 Hz, allowing a response and recovery time of less than 0.388 s and 1.171 s, respectively. This work introduces a fresh and cost-effective approach for developing lab-on-fiber concept-based sensors.** 

https://doi.org/10.1364/OL.500699

Relative humidity (RH) is critical in biomedicine, environmental science, agriculture, and food processing. Thus, the high-precision measurement of RH is significant for such practical applications. Electronic hygrometers are traditional solutions that have been widely deployed [1]. The increasing demand for more stringent humidity measurements has imposed higher requirements on humidity sensors, namely, higher sensitivity, faster response, and more stable repeatability. Thus, fiber optic humidity sensors based on fiber gratings [2] and interferometric methods [3] have received extensive attention recently. The fiber humidity sensors exhibit several advantages in better sensing performances, electromagnetic resistance, and multiplexing capability than the electronic hygrometers. Under the conceptual framework of the lab-on-fiber, functional-material-integrated all-in-fiber miniaturized probes have become a potential candidate for a novel generation of advanced all-in-fiber miniaturized probes [4]. Fabry–Perot interferometer (FPI) with a typically reflective designing framework has a more compact structure and is much more suitable for realizing lab-on-fiber technologies [5].

In previous works, much effort has been devoted to constructing functional FPI cavities on a fiber end, with core-offset splicing [6] and air-bubble blowing [7] being cost-effective techniques. However, all silica fiber structures are almost insensitive to RH. Besides, femtosecond-laser 3D printing is an advanced technique for growing FPIs on a fiber end. In this technique, the volume of the special polymer photoresist changes with the ambient RH, resulting in cavity length variation [3]. Given that the expensive equipment and the poisonous photoresistance used in the experiment have severely limited the popularization of this technology in constructing fiber-end FPIs, it is necessary to develop fiber-end FPIs considering both the cost and the sensitivity for RH sensing applications. The three-component solution contains a monomer-pentaerythritol diacrylate (PETIA), a sensitizing system (eosin Y), and a methyl diethanolamine, posing an innocuous photopolymerizable system [8]. When eosin is irradiated by a laser, the triplet state of eosin reacts with the amine to initiate the polymerization of the acrylate monomer [8]. The hydrophilic functional group in the acrylate expands the polymer as it absorbs water molecules [5]. Additionally, the thermal expansion effect of such a polymer is relatively low [9]. Therefore, it is a potential candidate for developing FPI-based sensors.

This Letter introduces a novel fiber-end photopolymerization (FEP) technique to construct FPI on a fiber end for measuring the RH in real-time. Specifically, the photopolymerizable solution is exposed to a 520 nm laser through a spatial mask served by the planetary core of a seven-core fiber (SCF). Two RH-sensitive polymer pillars grow from the fiber end. Similarly, an end cap is fabricated, exposing the commercially available UV adhesive to a UV laser through a multimode fiber (MMF) mask. The two pillars and the end cap are assembled to generate a laser-induced micro-cavity FPI (LIMC-FPI) sensor for RH measurement. Then, the RH response and the potential capacity for human breathing monitoring are characterized. Compared with traditional FPIs, the proposed LIMC-FPI exhibits attractive advantages in high sensitivity, ultra-compact structure, low cost, and quick response. Promising future applications of the

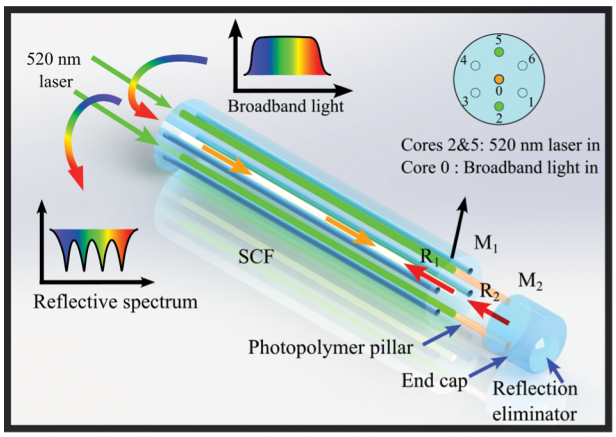


**Fig. 1.** Schematic diagram of the proposed LIMC-FPI.

proposed idea are respiratory humidity monitoring, agricultural production, and pharmaceutical engineering.

Figure 1 illustrates the schematic diagram of the LIMC-FPI. The micro-cavity, which comprises two humidity-sensitive polymer pillars and an end cap, is constructed on the end face of an SCF. The SCF/air and air/end cap interfaces are mirror 1 ($M_1$) and mirror 2 ($M_2$), respectively. A small glue drop on the other end face of the cap weakens the undesired reflective light and plays the role of a reflection eliminator. Therefore, two reflected beams couple back to the central core (core 0) of the SCF and interfere with each other, forming an extrinsic FPI. The wavelength of the destructive interference is expressed as [10]

$$\lambda_m = \frac{4\pi nL}{(2m+1)\pi}, \tag{1}$$

where $\lambda_m$ expresses the central wavelength of the $m^{th}$ order dip of the interference signal and $n$ refers to the refractive index (RI) of the air cavity, set to $n = 1$. $L$ is the cavity length, which is equal to the pillar length. The free spectral range (FSR), depicting the wavelength pitch between the adjacent dips, is expressed as [10]

$$FSR = \frac{\lambda_m^2}{2nL}. \tag{2}$$

FSR is inversely proportional to the cavity length $L$. To achieve a wider dynamic range, FSR must expand sufficiently. For the proposed LIMC-FPI, $L$ is determined by the initial length of the pillars depicted in Fig. 1. The sensitivity ($S$) of the LIMC-FPI, which refers to the relationship between $\lambda_m$ and RH, is derived by taking the partial derivative concerning RH at both ends of (1), as follows [5]:

$$S = \frac{d\lambda_m}{dRH} = \frac{4}{2m+1}\left(L\frac{dn}{dRH} + n\frac{dL}{dRH}\right). \tag{3}$$

When a certain dip is selected, $m$ is a constant. Both changes in the cavity length ($L$) and the RI of the medium in the cavity ($n$) with RH contribute to the sensitivity. For LIMC-FPIs, the length of the cavity increases as the polymer pillars absorb water, i.e., $dL/dRH>0$. However, the RI of air in the cavity is almost unchanged with RH [11]. Hence, $dn/dRH \approx 0$. Thus, we have

$$S = \frac{4}{2m+1}\frac{dL}{dRH}. \tag{4}$$

Equation (4) indicates that for a certain wavelength, the RH sensitivity $S$ is proportional to $dL/dRH$, which is the moisture expansion coefficient determined by the photopolymer.

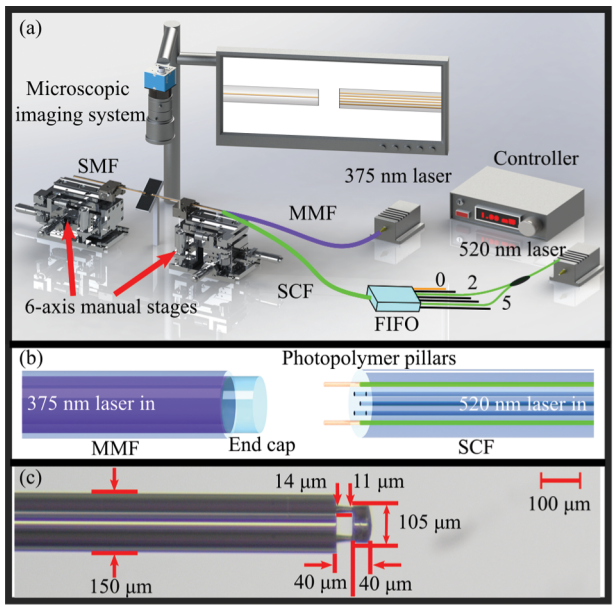


**Fig. 2.** (a) Experimental setup for fabricating LIMC-FPI. (b) Schematic diagram of the photopolymer pillars and the end cap. (c) Micrograph of the LIMC-FPI.

In addition to sensitivity, cavity finesse ($F$) and figure of merit (FoM) are two other important indicators in practical applications, defined by Eqs. (5) and (6), respectively [10]:

$$F = \frac{FSR}{2\lambda_{1/2}}, \tag{5}$$

$$FoM = \frac{S}{\lambda_{1/2}}, \tag{6}$$

where $2\lambda_{1/2}$ refers to the full width at half maximum (FWHM) of the cavity resonances, obtained by approximating the resonance line shapes using Lorentzian functions.

A novel three-step FEP technique is applied for fabricating the LIMC-FPIs.

Firstly, the SCF end of a fan-in/fan-out device (FIFO) OWMCF (Optoweave Co., Ltd.) is prepared and mounted on a 6-axis manual stage NFP-6561 (Zolix Instruments Co., Ltd.). The core diameter and pitch of the SCF are 8.2 μm and 42 μm, respectively. An SMF with a flat end face is mounted on another NFP-6561 and aligned with the SCF using two-dimensional machine vision. The photopolymerizable solution is dripped into the space between the SCF and the SMF. Then, we injected a 520 nm laser into cores 2 and 5 of the SCF through the FIFO, as illustrated in Fig. 2(a). Two polymer pillars grow from the end of cores 2 and 5 of the SCF due to the "self-trapping effect" [12]. It is worth noting that the output profile from a single core of the SCF is a well-known Gaussian-like distribution with energy decreasing gradually from the center to the edge. The photopolymerization occurs only if the laser energy density exceeds the reaction threshold [8]. Therefore, a higher input power increases the mode field diameter beyond the threshold, which increases the pillar diameter. The exposure time affects the length of the pillar. For longer pillars, it is necessary to increase the exposure time to allow sufficient polymerization. Due to the energy loss of the laser when propagating in the solution, the diameter at the end of the pillar is smaller than that near the SCF end face, giving the pillar the shape of the frustum of a cone. Although

there are high-order modes when the 520 nm laser propagates in the SCF, we still obtain an approximate Gaussian-like emission field using mechanical scrambling and realize quasi-cylindrical pillars [13]. The unreacted solution is washed off by alcohol. The schematic diagram of the photopolymer pillars is illustrated in Fig. 2(b).

Secondly, we replaced the SCF with a section of MMF, whose core/cladding diameter is 105 μm/125 μm. A 375 nm laser (MW-GC-380, Laser Optoelectronics Technology Co., Ltd.) with a pigtail output coupled UV laser is put into the MMF to cure the UV adhesive (NOA61, Norland Products Inc.) between the MMF end and the assisted SMF. A mechanical scrambler is still applied to generate a Gaussian-like emission field and make the end cap cylindrical. After 5 min of exposure, the end cap is obtained as depicted in Fig. 2(b). The uncured adhesive is washed off by acetone.

Thirdly, we dip a little NOA61 adhesive into the front of the polymer pillars. The end cap is aligned and attached to the pillars with the help of the machine vision and 6-axis manual stages. After exposing the structure to a UV lamp for 5 min, the end cap is integrated with the pillars, forming an air cavity at the end of the SCF. We add a small glue drop using a tapered fiber to eliminate the possible complex spectrum caused by the reflections from another end face of the end cap.

According to Eqs. (2) and (4), the initial length of the air cavity (also the length of the pillars) defined as $L_{ac}$ only affects the dynamic range by determining the FSR of the interference signal, without affecting the RH sensitivity. The end cap length $L_{ec}$ does not contribute to the dynamic range or sensitivity. Therefore, only the preparation feasibility and dynamic range must be considered for selecting the structural parameters of LIMC-FPI. The tentative experiments show that an optimum $L_{ec}$ is 40 μm. Indeed, a longer end cap will reduce the device's stability. While a shorter one is more likely to produce multi-beam interference, which causes a complex spectrum. Pillars shorter than 70 μm but longer than 30 μm consider the dynamic range and preparability. Figure 2(c) presents the micrograph of a LIMC-FPI with a cavity length ($L_{ac}$) and an end cap length ($L_{ec}$) of 40 μm and 40 μm, respectively. The diameters of the two ends of the pillars are 14 μm and 11 μm.

The reflective spectra of the four LIMC-FPIs with $L_{ec}$ of 40 μm and $L_{ac}$ of 40 μm to 70 μm are depicted in Fig. 3, indicating the corresponding FSR and $F$. The increase in cavity length decreases the FSR, with the results agreeing with Eq. (2). The maximum value of $F$ reaches 4.44, which is close to the recognized high finesse($F$>4.5) [10]. Since we only grow two pillars, the relative unevenness of the two mirrors will degrade $F$.

We then characterize the RH response of the four LIMC-FPI samples using the setup presented in Fig. 4(a). A supercontinuum laser source (SCL) SC-5 (YSL Photonics Co., Ltd.) injects broadband light ranging from 1400 nm to 1600 nm to core 0 through an optical circulator (OC) and the FIFO. The optical spectrum analyzer (OSA) AQ6370D (YOKOGAWA Co., Ltd.) records the reflected spectrum. Besides, the LIMC-FPIs are deployed in a temperature humidity chamber (THC) together with a thermohygrometer (THM) L95-2+ (LuGe Technology Co., Ltd.).

The RH in the THC increases from 30% to 90%, while the temperature is maintained at 30 °C. The spectral evolution of the LIMC-FPIs during the RH variation process is recorded, and the RH responses of the LIMC-FPI are calculated by tracing the wavelength shift of the target dip. Considering the compatibility

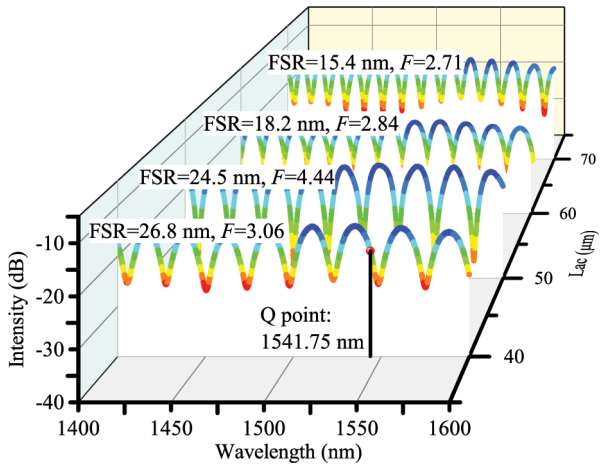


**Fig. 3.** Reflective spectra of the LIMC-FPIs with $L_{ac}$ of 40–70 μm.

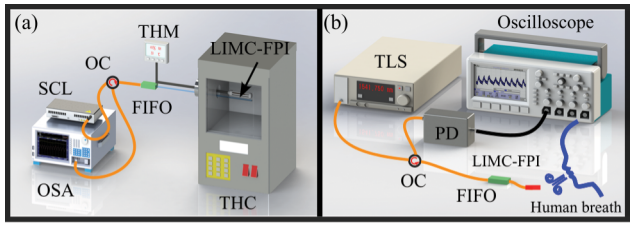


**Fig. 4.** Experimental setup for (a) measuring RH and (b) monitoring human breathing.

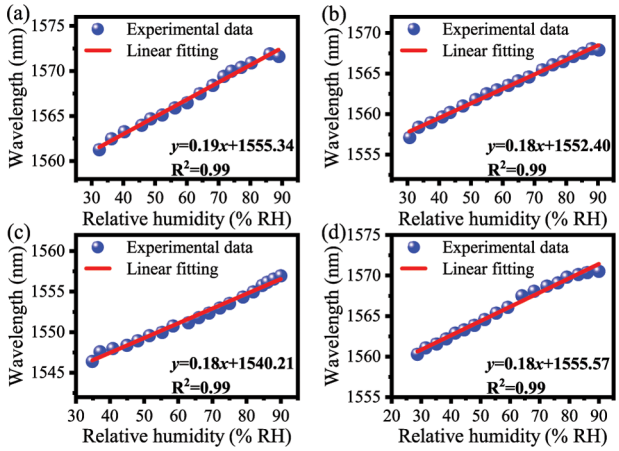


**Fig. 5.** RH response of the LIMC-FPI with (a) $L_{ac}$=40 μm; (b) $L_{ac}$=50 μm; (c) $L_{ac}$=60 μm; and (d) $L_{ac}$=70 μm.

with communication bands and the ease of spectral demodulation, dips around 1550 nm are selected and traced. The results are depicted in Fig. 5.

The target wavelength has a linear relationship with the ambient RH. As the humidity increases, more water vapor molecules are absorbed into the polymer pillars, increasing the length of the pillars. Therefore, target dips exhibit a significant redshift as they expand in the micro-cavity length. The RH sensitivity of sample 1 with $L_{ac}$ of 40 μm is calculated to be 0.19 nm/%RH, while 0.18 nm/%RH for the rest three in the RH range of 30%RH to 90%RH. The experimental results

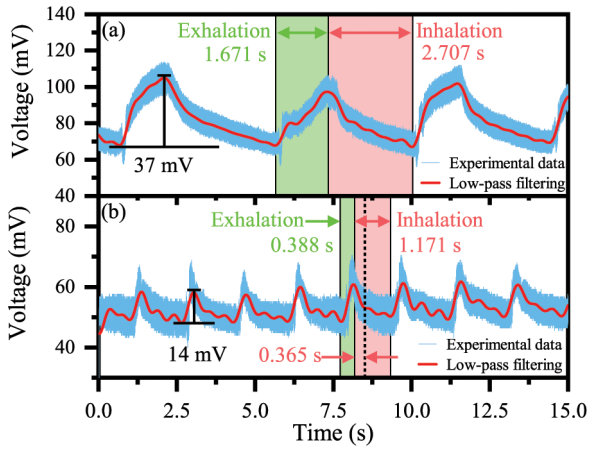


**Fig. 6.** Responses of the LIMC-FPI to human breath cycles. (a) Normal breathing. (b) Rapid breathing.

agree with Eq. (4), proving that the sensitivity of LIMC-FPI is independent of the cavity length and verifies the device's repeatability. The highest and average FoMs of the four samples are 0.07 /%RH and 0.058 /%RH, respectively. The LIMC-FPI are competitive in cost, sensitivity, structure size, and dynamic range compared with recently reported fiber humidity sensors [2,14,15].

The humidity response and recovery time are important indexes to evaluate the capability of online RH monitoring. We use the LIMC-FPI with $L_{ac}$ of 40 μm and $L_{ec}$ of 40 μm to monitor normal and rapid human breathing. The experimental setup is presented in Fig. 4(b). Specifically, a tunable laser source (TLS) MLS-2100 (Santec Holdings Corporation) injects a 1541.750 nm laser, which is the well-known working point (Q point shown in Fig. 3) for intensity demodulation [16], to the LIMC-FPI through the OC and FIFO. The reflected signal is collected by a photodetector (PD) and recorded by an oscilloscope DPO2014 (TEKTRONIX, INC.). The output voltage variation of PD during breathing is presented in Fig. 6.

A low-pass filter removes the high-frequency component noise caused by TLS power fluctuation. In normal breathing cycles with a frequency of 0.2 Hz, humidity accumulates with the exhalation process, sharply increasing the PD output voltage. During inhalation, the fast gas flow rate leads to the moisture evaporating rapidly, thus quickly decreasing the RH and the voltage. The result in Fig. 6(a) shows that the volunteers' exhalation and inhalation lasted 1.671 s and 2.707 s, respectively. We also characterize the device's response time by measuring the voltage rise time during rapid breathing (with a frequency of 0.5 Hz), as illustrated in Fig. 6(b). The PD output voltage maximizes within 0.388 s in a fast inhalation process. Considering the noise interference of the detector signal and the actual humidity accumulation time during rapid exhalation, we conclude that the humidity response time of LIMC-FPI is less than 0.388 s. It is worth noting that the PD output voltage drops rapidly during inhalation, requiring about 0.365 s. Then, the voltage gradually drops back to the initial level. The entire recovery process lasts 1.171 s. In addition, the change in PD output voltage during rapid breathing (14 mV) is lower than that in the normal breathing process (37 mV). This is because the actual RH variation during rapid breathing is lower than normal breathing.

In conclusion, this Letter realized a lab-on-fiber concept by constructing a micro-cavity on a fiber end for online humidity sensing. A novel fiber-end photopolymerization technique is applied for fabricating the device. As a 520 nm laser exits from a pair of symmetric cores, the laser-induced polymerization occurs, forming two humidity-sensitive pillars. After manufacturing an end cap using a multimode fiber mask and integrating it with the pillars, we obtain a LIMC-FPI on the fiber end. The polymer pillars absorb water molecules, increasing the cavity length. Experimental results indicate that the repeatable humidity sensitivity of the LIMC-FPI reaches 0.18 nm/%RH with a maximum FoM of 0.07 /%RH. The suggested device is responsive in the breathing frequency range of 0.2 Hz to 0.5 Hz. The response and recovery time is faster than 0.388 s and 1.171 s, respectively. The sensitivity and the response time are competitive among the reflective-type fiber humidity sensors. The LIMC-FPI also has an ultra-compact structure with a sensing region of only 80 μm. The proposed method applies to environmental or biological RH sensing within a restricted space.

**Funding.** National Key Research and Development Program of China (2020YFB2009203); the Joint Research Fund in Astronomy under cooperative agreement between the National Natural Science Foundation of China (NSFC) and Chinese Academy of Sciences (CAS) (U2031130, U2031132); the State Key Laboratory of Applied Optics (SKLA02022001A02); the Fundamental Research Funds for the Central Universities to the Harbin Engineering University (3072022QBZ2501).

**Disclosures.** The authors declare no conflicts of interest.

**Data availability.** Data underlying the results presented in this paper are not publicly available at this time but may be obtained from the authors upon reasonable request.

## REFERENCES

1. X. Y. Meng, J. H. Yang, Z. G. Liu, W. B. Lu, Y. M. Sun, and Y. Q. Dai, Comp. Commun. **20**, 100347 (2020).
2. K. Zhu, X. Cheng, Z. Y. Zhao, and C. Lu, Opt. Lett. **45**, 6603 (2020).
3. D. Liu, Z. H. Cai, B. Z. Li, M. Q. Zou, L. C. Zhang, Y. Z. Hua, J. H. Mai, C. Zhao, C. R. Liao, J. He, X. Y. Weng, L. W. Liu, J. L. Qu, and Y. P. Wang, Opt. Express **31**, 8738 (2023).
4. A. Ricciardi, A. Crescitelli, P. Vaiano, G. Quero, M. Consales, M. Pisco, E. Esposito, and A. Cusano, Analyst **140**, 8068 (2015).
5. Z. X. Hu, Y. X. Chen, J. Y. Tan, Z. Y. Yan, Z. H. Weng, M. Gusain, Y. Q. Zhan, and L. M. Xiao, Sens. Actuators, B **346**, 130462 (2021).
6. Z. H. Li, L. K. Li, Y. N. Zhang, B. Han, J. C. Zhao, X. G. Li, and Y. Zhao, Opt. Fiber Technol. **74**, 103148 (2022).
7. B. N. Liu, J. X. Luo, S. Liu, Y. P. Chen, B. Huang, C. R. Liao, and Y. P. Wang, Photonic Sens. **11**, 411 (2021).
8. A. Espanet, C. Ecoffet, and D. J. Lougnot, J. Polym. Sci. A Polym. Chem. **37**, 2075 (1999).
9. Z. H. Shen, R. W. Yu, Y. X. Chen, C. Y. Wang, W. Chen, L. Y. Liu, L. Xu, and L. M. Xiao, J. Lightwave Technol. **41**, 4322 (2023).
10. D. Aydin, J. A. Barnes, and H. P. Loock, Appl. Phys. Rev. **10**, 1 (2023).
11. H. Golnabi, Opt. Lasers Eng. **50**, 1495 (2012).
12. P. Gustafik, O. Sugihara, and N. Okamoto, Jpn. J. Appl. Phys. **43**, 2011 (2004).
13. L. M. Xiao, W. Jin, and M. S. Demokan, Proc. SPIE **6379**, 637902 (2006).
14. Z. H. Liu, M. Zhang, Y. Zhang, Y. X. Zhang, K. Q. Liu, J. Z. Zhang, J. Yang, and L. B. Yuan, Opt. Lett. **44**, 2907 (2019).
15. Y. Zhao, R. J. Tong, M. Q. Chen, and F. Xia, Sens. Actuators, B **284**, 96 (2019).
16. S. Liu, W. Q. Yan, J. L. Zhong, T. Zou, M. Zhou, P. J. Chen, H. Xiao, B. A. Liu, Z. Y. Bai, and Y. P. Wang, Sens. Actuators, B **369**, 132372 (2022).